

## Structural changes and conductance thresholds in metal-free intrinsic SiO<sub>x</sub> resistive random access memory

Adnan Mehonic, Mark Buckwell, Luca Montesi, Leon Garnett, Stephen Hudziak, Sarah Fearn, Richard Chater, David McPhail, and Anthony J. Kenyon

Citation: *Journal of Applied Physics* **117**, 124505 (2015); doi: 10.1063/1.4916259

View online: <http://dx.doi.org/10.1063/1.4916259>

View Table of Contents: <http://scitation.aip.org/content/aip/journal/jap/117/12?ver=pdfcov>

Published by the [AIP Publishing](#)

---

### Articles you may be interested in

[Cu impurity in insulators and in metal-insulator-metal structures: Implications for resistance-switching random access memories](#)

*J. Appl. Phys.* **117**, 054504 (2015); 10.1063/1.4907578

[Characterization of external resistance effect and performance optimization in unipolar-type SiO<sub>x</sub>-based resistive switching memory](#)

*Appl. Phys. Lett.* **105**, 133501 (2014); 10.1063/1.4896877

[Intrinsic SiO<sub>x</sub>-based unipolar resistive switching memory. II. Thermal effects on charge transport and characterization of multilevel programing](#)

*J. Appl. Phys.* **116**, 043709 (2014); 10.1063/1.4891244

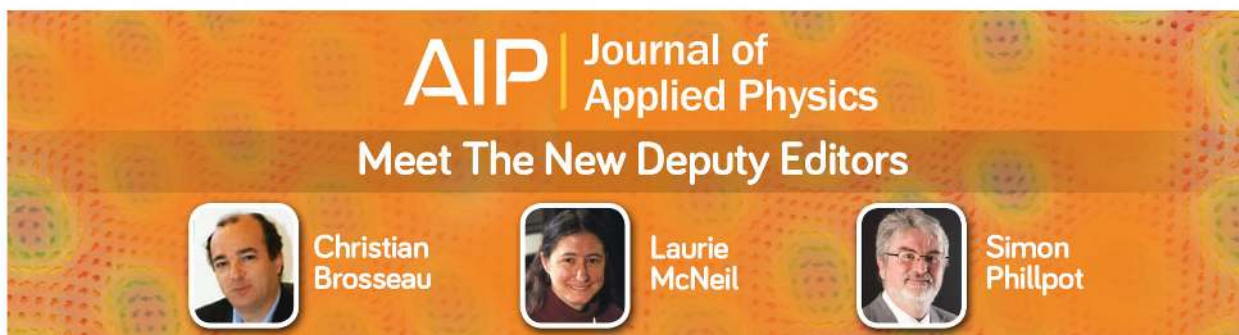
[Intrinsic SiO<sub>x</sub>-based unipolar resistive switching memory. I. Oxide stoichiometry effects on reversible switching and program window optimization](#)

*J. Appl. Phys.* **116**, 043708 (2014); 10.1063/1.4891242

[The x dependent two kinds of resistive switching behaviors in SiO<sub>x</sub> films with different x component](#)

*Appl. Phys. Lett.* **104**, 012112 (2014); 10.1063/1.4861592

---



## Structural changes and conductance thresholds in metal-free intrinsic SiO<sub>x</sub> resistive random access memory

Adnan Mehonic,<sup>1,a)</sup> Mark Buckwell,<sup>1</sup> Luca Montesi,<sup>1</sup> Leon Garnett,<sup>1</sup> Stephen Hudziak,<sup>1</sup> Sarah Fearn,<sup>2</sup> Richard Chater,<sup>2</sup> David McPhail,<sup>2</sup> and Anthony J. Kenyon<sup>1,a)</sup>

<sup>1</sup>Department of Electronic and Electrical Engineering, UCL, Torrington Place, London WC1E 7JE, United Kingdom

<sup>2</sup>Department of Materials, Imperial College London, South Kensington Campus, London SW7 2AZ, United Kingdom

(Received 25 January 2015; accepted 14 March 2015; published online 25 March 2015)

We present an investigation of structural changes in silicon-rich silicon oxide metal-insulator-metal resistive RAM devices. The observed unipolar switching, which is intrinsic to the bulk oxide material and does not involve movement of metal ions, correlates with changes in the structure of the oxide. We use atomic force microscopy, conductive atomic force microscopy, x-ray photoelectron spectroscopy, and secondary ion mass spectroscopy to examine the structural changes occurring as a result of switching. We confirm that protrusions formed at the surface of samples during switching are bubbles, which are likely to be related to the outdiffusion of oxygen. This supports existing models for valence-change based resistive switching in oxides. In addition, we describe parallel linear and nonlinear conduction pathways and suggest that the conductance quantum,  $G_0$ , is a natural boundary between the high and low resistance states of our devices. © 2015 AIP Publishing LLC. [<http://dx.doi.org/10.1063/1.4916259>]

### I. INTRODUCTION

Non-volatile memories exploiting resistive switching<sup>1</sup>—resistive RAM (RRAM) devices—offer the possibility of low programming energy per bit,<sup>2</sup> rapid switching,<sup>3</sup> and very high levels of integration—potentially in 3D.<sup>4</sup> The ultimate technological goal is to overcome the limitations of next generation flash memories—speed, power dissipation, and scaling. Resistive switching in a silicon-based material offers a compelling alternative to existing metal oxide-based devices (e.g., HfO<sub>2</sub> and TiO<sub>2</sub>), being fully CMOS-compatible. Recent reports of silicon oxide based RRAM include electrochemical metallization (ECM) RRAM (also known as conductive bridge RAM or CBRAM), in which a silicon-rich silica (SiO<sub>x</sub>) matrix supports the drift of metallic ions from an electrochemically active electrode; the matrix does not play an active role in the switching process.<sup>5</sup> Alternatively, the silicon oxide may be doped with metallic species during fabrication;<sup>6–8</sup> metal ions can drift under the application of an external field to form a conductive bridge between the electrodes. Both approaches can be thought of as *extrinsic* switching. Very few papers, however, have reported *intrinsic* resistive switching in metal-free silicon oxide. In fact, there have been statements in the literature that suggest that intrinsic resistive switching in silicon oxide is not possible.<sup>9</sup> Nevertheless, there is a long history of research into resistance changes in silicon oxide. Early work dates back to the 1960s and 1970s, at which time the irreversible electrical breakdown of silicon dioxide was at the forefront of interest as integrated microelectronics technology was maturing.<sup>10–12</sup> More recently, there have been several reports of *reversible*

dielectric breakdown, or so-called *soft* breakdown, of silicon oxide. Some works, notably that of Tour's group at Rice University,<sup>13</sup> focus on surface-based mechanisms in which silicon conductive filaments form at exposed oxide edges. A similar surface-based mechanism is reported in other studies.<sup>14,15</sup> However, the switching mechanism in such studies is fundamentally different to that in reports, including ours<sup>2,16</sup> and subsequent reports,<sup>17–19</sup> which concentrate on intrinsic conductivity changes in bulk silicon oxide. Of particular note are two points: first, surface switching can operate only under vacuum conditions, while bulk switching is stable in ambient and, therefore, does not require the hermetic sealing of devices that is required to prevent the rapid oxidation of silicon filaments formed at oxide surface. Second, the Rice group report reset voltages that are higher than the corresponding set; in our devices, in contrast, set occurs at the higher voltage. This suggests a wholly different switching mechanism.

In this paper, we study intrinsic resistive switching in metal-free SiO<sub>x</sub> MIM (metal-insulator-metal) structures. Such a structure has been investigated in Ref. 17, while comprehensive studies of both surface and bulk based switching are presented in Refs. 18 and 19. In this paper, we analyse and put a special focus on structural changes resulting from switching, using Atomic Force Microscopy (AFM), Conductive Atomic Force Microscopy (C-AFM), X-ray Photoelectron Spectroscopy (XPS), and Secondary Ion Mass Spectroscopy (SIMS).

We also investigate linear and nonlinear components of device conduction, highlighting the importance of the conductance quantum,  $G_0 = 2 e^2/h$  as a natural boundary between the high and low resistance states of devices.

<sup>a)</sup>Electronic addresses: a.mehonic@ee.ucl.ac.uk and t.kenyon@ucl.ac.uk

## II. EXPERIMENTAL DETAILS

### A. Device fabrication

MIM RRAM structures were fabricated as follows: p-Si wafers with a top pre-processed 4  $\mu\text{m}$ -thick thermal  $\text{SiO}_2$  layer were used as the substrate. The bottom electrode of the devices consisted of a 100 nm thick layer of TiN deposited by magnetron co-sputtering at room temperature.  $\text{SiO}_x$  layers (37 nm thick) were sputtered at 250  $^\circ\text{C}$  using  $\text{SiO}_2$  and Si confocal cathodes in an Ar plasma. Excess silicon content was 11 at. %. The silicon excess was estimated using XPS. Samples were annealed at 600  $^\circ\text{C}$  post-deposition in Ar. A top layer of TiN, identical to that used for the bottom electrode (i.e., 100 nm thick), was deposited and electrode structures formed by standard photolithography. Various square electrode pads were formed, with sizes ranging from 400  $\mu\text{m}$  to 5  $\mu\text{m}$  square.

### B. Measurements

Devices were characterised electrically using a Keithley Instruments 4200S semiconductor parameter analyser and a Signatone probe station with 10  $\mu\text{m}$  tip diameter tungsten probes. XPS measurements were performed using a Thermo Scientific K-Alpha with a monochromated Al source at  $10^{-8}$  Torr. An elliptical x-ray illumination spot with a major axis of 400  $\mu\text{m}$  at 1486.68 eV was used to gather data and the analyser pass energy was set at 20 eV. Spectra were calibrated using the carbon C1s peak. Spectral data were processed using CasaXPS v2.3.16. SIMS data were obtained using ION-TOF ToF-SIMS instrumentation. Samples were sputtered with a 1 keV, 65 nA  $\text{Cs}^+$  beam for depth profiling and a 25 keV  $\text{Bi}^+$  was used for secondary ion generation. AFM and C-AFM measurements were carried out using a Bruker Icon microscope with a NanoScope V Controller.

C-AFM measurements were performed with a Pt/Ir-coated silicon cantilever with a sample bias of 10 V (C-AFM tip grounded) and series resistance of 178 k $\Omega$ .

## III. RESULTS AND DISCUSSION

### A. Device fabrication

Figure 1(a) shows I-V curves with an initial electroforming step into a low resistance state at  $\sim 6$  V, and subsequent reset and set processes at approximately 2.5 V and 3 V, respectively. The initial forming process can be achieved equally well in the negative bias. In contrast to the MOS devices we have studied previously,<sup>2,16</sup> the structural symmetry of the MIM structure results in typical unipolar switching. In our devices, the set voltage is centred around 3.5 to 4 V, while the reset voltage is typically about 2.5 V. On the contrary, Yao *et al.* report unipolar switching in  $\text{SiO}_x$  mesa structures in which the reset voltage is higher than the set.<sup>13</sup> Significantly, the authors of that study cannot produce switching away from an exposed oxide surface. These observations together suggest, as outlined in our introduction, that the mechanism of switching reported by Yao *et al.*—the formation of Si conductive filaments on the surface of the  $\text{SiO}_x$ —is not that reported here (conductive filament formation and disruption in bulk oxide), and hence the electrical characteristics are very different.

The pristine state of the switching oxide has a high resistance ( $\sim 10^9 \Omega$ ); under the application of modest fields, currents are typically in the nanoamp to microamp range (Figure 1(a) inset). However, following the application of a voltage stress above a critical level (6 V in the case of Figure 1(a)) with a current compliance limit set to avoid destructive dielectric breakdown, the device enters a much lower resistance state in which currents are defined by the current compliance limit (3 mA in this case). This is the

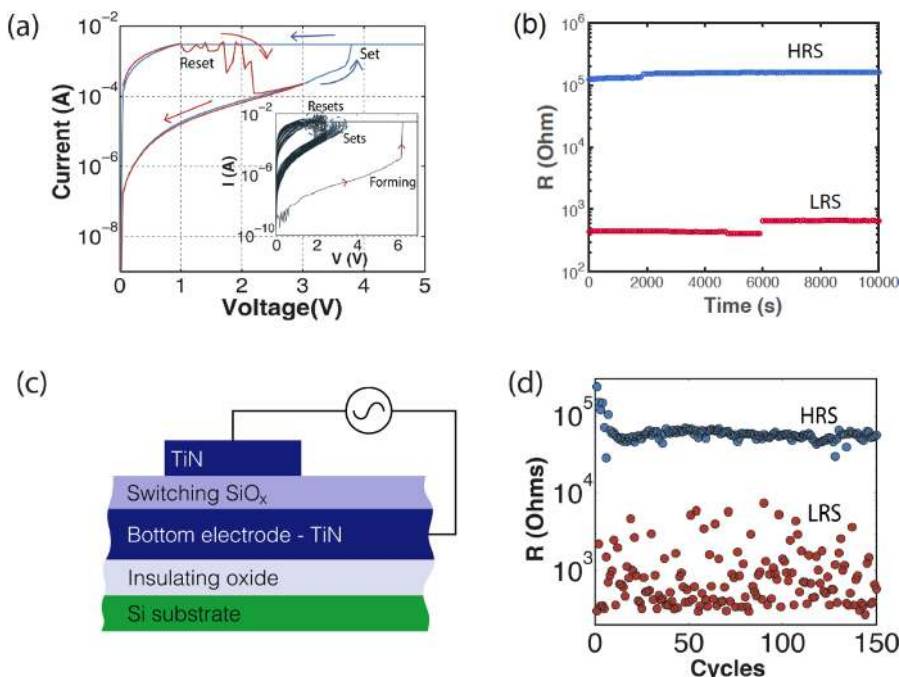


FIG. 1. (a) I-V curve showing resistive switching with a typical contrast ratio of 150. Right inset: I-V curves showing resistive switching and the forming process. (b) Retention test over  $10^4$  s. (c) Device schematic. (d) Endurance testing—150 cycles, recording every cycle.

forming step. Removal of the current compliance limit allows the device to be reset into a high resistance state whose resistance is intermediate between that of the set and pristine states. Such behaviour is indicative of partial disruption of the conductive filament created during the forming process—that is to say, the bulk of the filament remains, but oxidation of a single weak point breaks the conductive path. Residual conduction is by tunnelling across the oxidised gap or by background conduction through the partially formed tissue around the filament (see below). This is the conventional model for switching in redox-based oxide RRAM.

The set process is seen typically as a single abrupt jump to current compliance (3 mA), while the reset process shows several intermediate transitions, suggestive of a different switching mechanism. The inset shows 20 resistive switching I-V curves. We note that both the forming voltage and the programming voltages are significantly lower than those reported in our previous study of SiO<sub>x</sub> MOS (metal-oxide-semiconductor) RRAM devices,<sup>2,16</sup> and are similar to those reported for SiO<sub>x</sub> devices using conductive interlayers such as Pd, Ti, or carbon.<sup>20</sup> This is likely to be due to a combination of factors: the simpler device structure of MIM, with fewer interfaces, and the intrinsically higher conductivity of metallic electrodes. Similarly, set state (low resistance state) currents are higher for MIM than MOS (3 mA, compared with a few  $\mu$ A). Resistance states are stable over 10<sup>4</sup> s with a 0.5 V reading voltage applied every 100 s as shown in Figure 1(b). Between reading events, the device terminals are kept floating in an effort to emulate deployment in a digital computing environment. Figure 1(d) shows a representative set of 150 stable switching cycles that maintain a contrast between the states of at least one order of magnitude. States were changed with DC pulses with a length of about 1 s. Pulses were 15 V at 3 mA to form, 7 V at 3 mA to set, and 2.7 V (no compliance) to reset. Notice that compliance effectively shortens forming and setting pulses to the amount required to create or disrupt the filament. Programming pulses were followed by 1 V DC read pulses. During this test, a voltage of 0 V was imposed on the device between DC pulses. Note that we measured the device resistance after every set and reset pulse.

To investigate the spread of set and reset voltages, we accumulated data from three thousand set and reset processes from which we were able to generate cumulative probability plots for both transitions. Data were obtained for 100  $\mu$ m, 200  $\mu$ m, and 400  $\mu$ m square electrodes to investigate any dependence of switching voltage on electrode size. These results are presented in Figure 2. There is no observed dependence of switching voltage on device size. The resistances of the low resistive state (LRS) and high resistive state (HRS) do not scale with the device size, which is consistent with the filamentary model of switching. This is shown in Figures 2(b) and 2(c).

## B. XPS and SIMS characterisation

In the case of metal oxide RRAM switches, the set and reset processes are associated with the formation and disruption of conductive filaments. The conventional model of

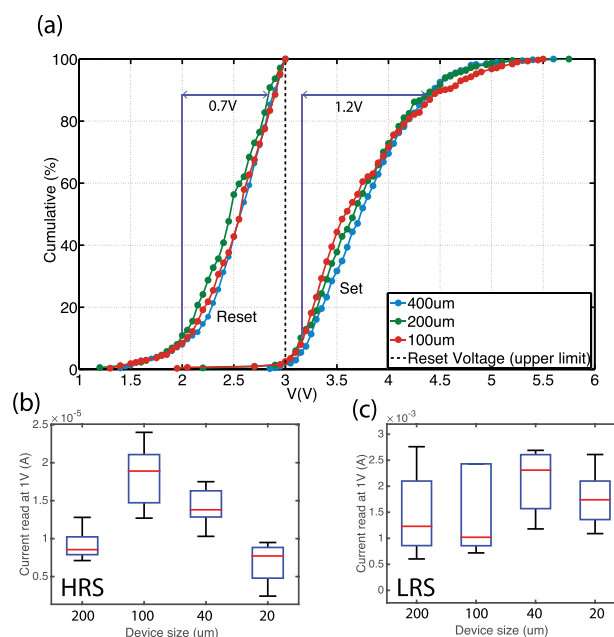


FIG. 2. (a) Cumulative probability plots of set and reset voltages for 100  $\mu$ m, 200  $\mu$ m, and 400  $\mu$ m contacts. Data were obtained for 3000 switching events. Resistance distribution dependence on electrode size in (b) HRS and (c) LRS. The line inside the box is the median value. The top and the bottom of the box represent the 25th and 75th percentiles, respectively. The two whiskers are the maximum and the minimum values of the state conductance. “Device size” refers to the edge length of the square electrodes.

switching in oxide RRAM is that of movement of oxygen ions inside the oxide matrix governing both forming and resistive switching. There are two drivers for this: an electric field across the dielectric matrix and Joule heating generated by the passing current; in real devices these processes act simultaneously. It is likely that a similar mechanism operates in our silicon oxide devices, and hence changes in resistance state should correlate with changes in oxide stoichiometry and structure.

To examine the changes in stoichiometry following the electroforming process, we used a 10  $\mu$ m diameter tungsten probe to directly stress the silicon oxide on a contact-free area. As the x-ray illumination area is much larger than a typical filament diameter, and also larger than the footprint of the probe, we produced a region of oxide containing a high density of conductive filaments by applying voltage sweeps to +25 V at points located at 40  $\mu$ m intervals in a grid-like layout across a 400  $\mu$ m square region. 25 V is a much higher voltage that is used in general device operation; it allowed us to overcome the additional energy barrier present due to native oxide growth on the surface of the silicon-rich oxide. To prevent overstressing, we set a 100  $\mu$ A current compliance limit.

It has been reported that the presence of the asymmetrical SiO<sub>2</sub>≡Si-Si and O<sub>3</sub>≡Si-Si configurations within pristine films enhances the formation of oxygen vacancies or dangling bonds under the application of an external field.<sup>17</sup> Our films are rich in these configurations, as shown by the XPS results from the bulk of the film (obtained by milling the surface layers using an argon ion beam to expose the bulk

material) presented in Figure 3(a). Deconvolution of the Si2p XPS peak confirms the presence of three silicon suboxide peaks, Si<sup>1+</sup>, Si<sup>2+</sup>, and Si<sup>3+</sup>, an elemental silicon peak, Si<sup>0</sup>, and Si<sup>4+</sup> peak indicative of fully oxidised silicon. This elemental silicon sub-peak is due to silicon nano-inclusions within the oxide layer, and its large contribution (24.4%) together with the small Si<sup>4+</sup> (i.e., SiO<sub>2</sub>) contribution (4.2%) confirms that the oxide is silicon-rich. The fitted peaks have binding energies (BE) and percentage contributions to the total spectrum, respectively, of 99.8 eV at 24.4% (Si<sup>0</sup>), 100.54 eV at 25.60% (Si<sup>1+</sup>), 100.5 eV at 25.2% (Si<sup>1+</sup>), 101.6 eV at 19.9% (Si<sup>2+</sup>), 102.7 eV at 26.3% (Si<sup>3+</sup>), and 103.8 eV at 4.2% (Si<sup>4+</sup>). The large contribution from Si<sup>3+</sup> suggests a high concentration of asymmetrical SiO<sub>2</sub>≡Si-Si and O<sub>3</sub>≡Si-Si species.

Figure 3(b) presents the O1s XPS spectrum of the SiO<sub>x</sub>, showing the presence of single (–O–) and peroxy (–O–O–) configurations of oxygen within the switching layer. These two fitted peaks have binding energies and percentage contributions of 532.2 eV at 64.1% (–O–) and 532.8 eV at 35.9% (–O–O–). The adjoining atoms to each oxygen configuration may be Si or H, presenting a broad selection of bonding arrangements, peroxy bridges and chain terminations in the oxide.

Figures 3(c) and 3(d) show the Si2p and O1s XPS spectra, respectively, for the SiO<sub>x</sub> film following electroforming. From Figure 3(c), it can be seen that silicon is reduced

following the electroforming process. This is demonstrated by the decrease of between 0.9% and 3.2% in contributions from oxidised silicon components (Si<sup>1+</sup>, Si<sup>2+</sup>, Si<sup>3+</sup>, and Si<sup>4+</sup>) and a concurrent 8.9% increase in elemental silicon inclusions, Si<sup>0</sup>. Further evidence for the dissociation of oxygen in the film is the 26% decrease in peroxy oxygen configurations, as shown in Figure 3(d), and the calculated overall 7% decrease in the total oxygen content. This suggests that peroxy configurations are, in particular, dissociated under electrical stress, leading to a loss of oxygen from the active layer.

The presence of hydrogen and peroxy-configurations of oxygen in the SiO<sub>x</sub> layer is confirmed by SIMS data (Figure 3(e)). Many arrangements of H, O, and Si are present in the switching layer, with notable accumulations at the edges of the active layer. This highlights the complex nature of the SiO<sub>x</sub> and, combined with the XPS spectra, demonstrates the structural disorder of the system and its tendency to dynamic behavior under stress.

### C. AFM, C-AFM

To examine the size and the location of the conductive filaments produced during the forming process, we again placed a 10 μm diameter tungsten probe tip directly onto the silicon oxide on a contact-free area and swept the voltage until the forming transition was seen. We then used atomic

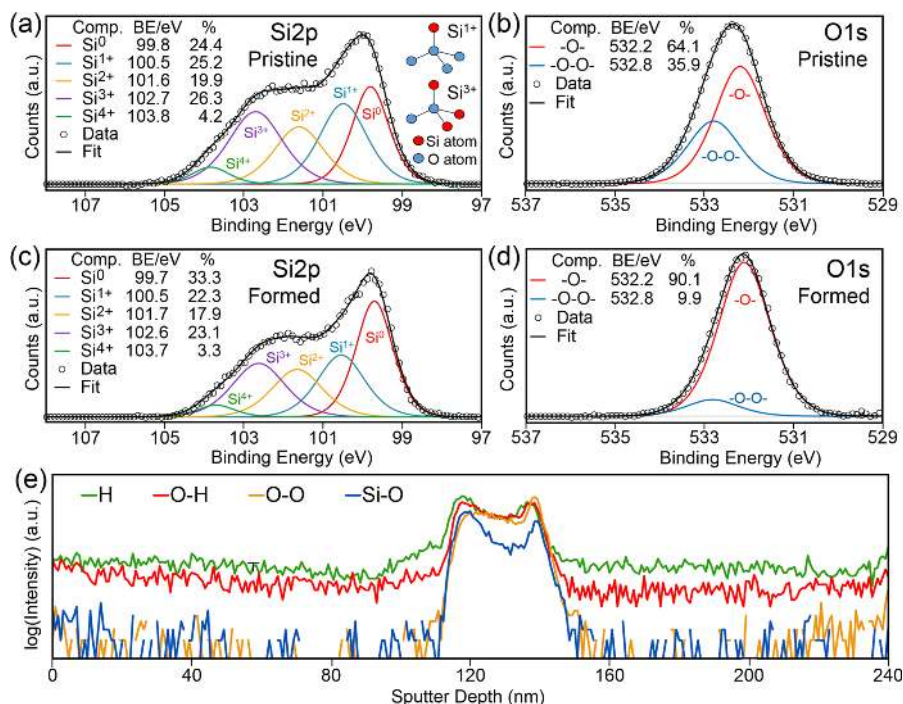


FIG. 3. (a) Si2p XPS spectrum of the pristine film, showing the presence of asymmetrical SiO<sub>2</sub>≡Si-Si and O<sub>3</sub>≡Si-Si (Si<sup>3+</sup>) configurations. (b) O1s XPS spectrum of the pristine film, showing the presence of oxygen in single (–O–) and peroxy (–O–O–) configurations. (c) Si2p XPS spectrum of the electroformed film, showing decreases in the suboxide (Si<sup>1+</sup>, Si<sup>2+</sup>, Si<sup>3+</sup>) and oxide (Si<sup>4+</sup>) contributions, with a corresponding increase in the presence of elemental silicon inclusions, Si<sup>0</sup>. (d) O1s XPS spectrum of the electroformed film, showing a decrease in the presence of peroxy configurations and increase in single oxygen atoms. Note that the O1s data have been scaled assuming a constant total silicon signal for each sample, resulting in a calculated 7% decrease in the total oxygen content of the film. During deconvolution of all XPS spectra, sub-peak components were allowed to shift by ±0.05 eV to account for experimental variation. Hence, in rounding the BE values for presentation, the maximum shift is ±0.1 eV. (e) SIMS depth profile through a pristine MIM device from the surface of the top electrode (0 nm) to the base of the bottom electrode (240 nm). The active layer spans from around 110 nm to 150 nm. A small selection of the diverse bonding configurations of H, O, and Si present in our SiO<sub>x</sub> is shown.

force microscopy and conductive atomic force microscopy to track both the structural evolution of the film surface and any corresponding spatially resolved conductivity changes.

While it is possible that forming and resistive switching by placing the tungsten tip on a contact free area may differ from that obtained by placing the tip on a TiN contact, this approach can nevertheless provide insight into structural changes that occur within the  $\text{SiO}_x$  layer during switching. In any case, we have previously reported resistive switching in  $\text{SiO}_x$  using the atomically sharp tip of a scanning tunneling microscope.<sup>2</sup>

We may form using either positive or negative biases applied to the oxide; in both cases, bubble-like structures appear on the surface of the  $\text{SiO}_x$  film (Figures 4(a) and 4(b)). Similar behaviour has been reported previously in  $\text{TiO}_2$  based RRAM devices, in which it has been suggested that the bubbles contain accumulated oxygen beneath the film surface resulting from  $\text{O}^-$  ion movement during forming.<sup>21,22</sup> The colour mapping in Figures 4(a) and 4(b) shows the surface rigidity of the area, normalized to pristine  $\text{SiO}_x$ , corresponding to the energy dissipation of the surface during force-distance scans of the AFM probe. Each pixel is generated by averaging 5 consecutive spectra at the same location, with the hysteresis in the approach and retract curves integrated to calculate the energy dissipated. More negative (red) values indicate that more energy has been dissipated than on the pristine (blue/green) material. This corresponds to the presence of a soft, elastic surface. Our C-AFM measurements (Figures 4(c) and 4(d)) additionally show that conductive regions appear characteristically to the side or edge of the bubbles. These regions may correspond to the tops of conductive filaments. Interestingly, as bubbles are observed in both bias polarities, it is likely that these surface features are partly a result of Joule heating as well as the applied field. In the case of the negative bias, the energy dissipated by the bubble decreases only by 15 keV from that of the surrounding oxide. There are also small neighbouring regions that show a positive change of up to 15 keV in dissipation, indicating the presence of a harder surface. However, in the

case of the positive bias the bubble dissipation is 60 keV: four times that of the negative bias.

It is notable that surface distortions are seen during electroforming in both bias polarities. In the case of a positive bias applied to the top surface, this may be explained by the field-driven movement of oxygen to the upper interface. Note that switching is unipolar, so the overall movement of oxygen may be dominated by thermal effects. In other words, switching is driven by thermochemical processes.<sup>22</sup> Thus, in the case of a negative bias, although oxygen will be driven by the field to the bottom interface, thermal processes will also play a major role and allow oxygen to move to the top surface. An important distinction between the two cases is the much greater softening of the surface seen in positive bias. This may be a different situation to that of bipolar devices in which switching and surface distortion are dominated by field effects.<sup>23</sup>

#### IV. SWITCHING MECHANISM

On the basis of our XPS and SIMS results, we suggest that, during the forming process, oxygen anions are generated by bond breakage within the asymmetric  $\text{SiO}_2 \equiv \text{Si}-\text{Si}$  and  $\text{O}_3 \equiv \text{Si}-\text{Si}$  configurations. This process may be encouraged by the presence of peroxy-bound oxygen atoms within the film, the splitting of which acts as a precursor to further breakage of silicon-oxygen bonds. Ions drift towards the top electrode leaving a percolation path consisting of oxygen vacancies that can support electron conduction. This is the set/forming process that switches the device to the LRS. During the reset process, under the thermally assisted migration of oxygen, part of the filament is re-oxidised, recovering the HRS. This process is shown schematically in Figure 5, and is described in the various different metal-oxide RRAM systems generally as a thermo-chemical (TCM) or valence-change mechanism (VCM).<sup>24</sup> Our results are consistent with the assumption that the movement of oxygen is at the heart of the switching process.

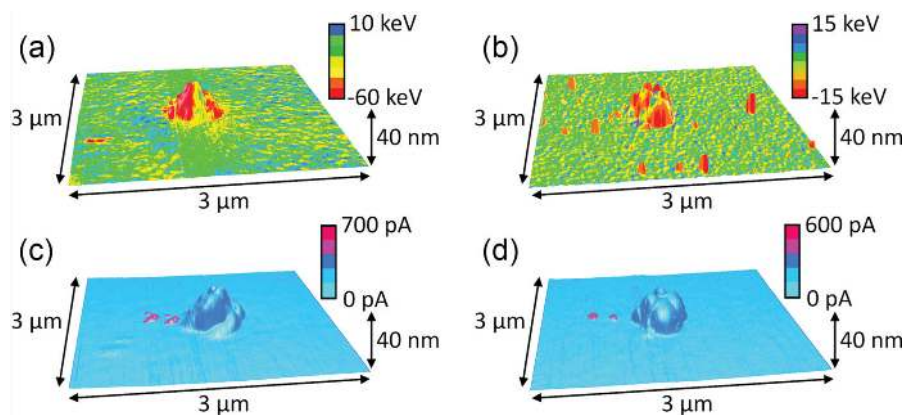


FIG. 4. (a) and (b) Quantitative Nanomechanical Property Mapping™ AFM scans of point-of-contact after positive and negative forming pulses, respectively. Note that the dispersed points of high dissipation (red) around the central feature are most likely debris present as a result of the surface deformation. Such loose material would have been measured during the energy dissipation scan but subsequently removed during contact-mode C-AFM scanning. (c) and (d) C-AFM scans showing both a bubble-like structure and associated regions of high conductivity (possible filament sites) for the areas shown in (a) and (b), respectively.

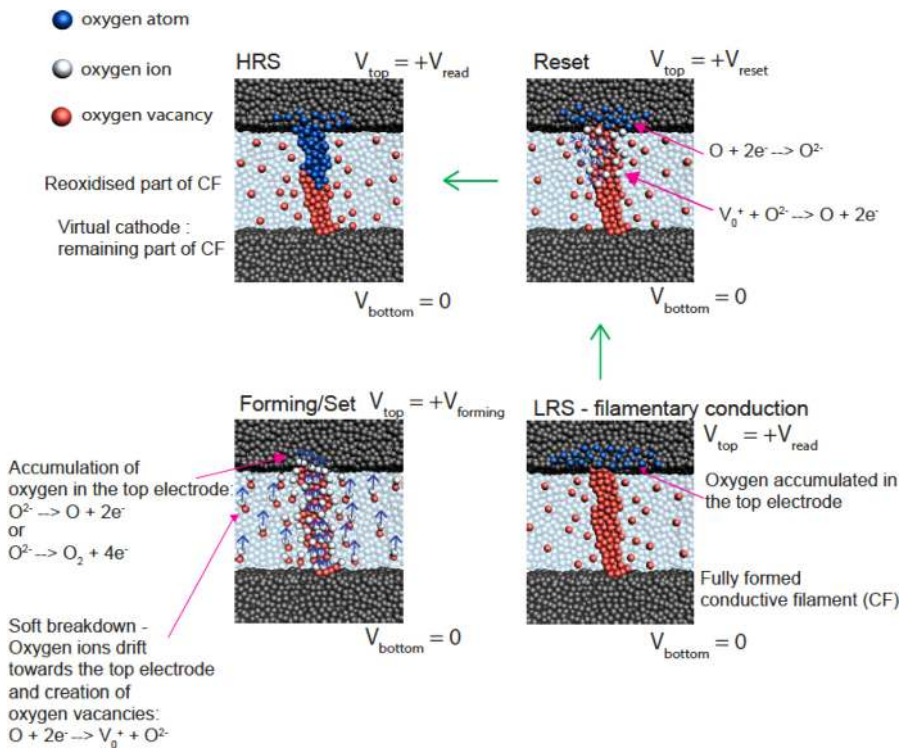


FIG. 5. Schematic of the switching process. Application of an appropriate voltage with a current compliance limit to the pristine device forms the oxide into a low resistive state (LRS) by moving oxygen ions to one of the electrodes, generating a conductive filament bridging the two electrodes as oxygen vacancies are left behind. Removing the current compliance and applying a suitable voltage then disrupts the filament through thermally assisted migration of oxygen, returning the device to a high resistive state (HRS).

We also note that we have observed resistive switching using different electrode configurations, including silicon electrodes—we reported a p-type silicon substrate as the bottom electrode and n-type poly silicon as the top electrode in our previous study.<sup>2</sup> This further confirms the intrinsic nature of the switching.

Having established that the MIM structures exhibit unipolar switching, and that this is accompanied by structural changes in the switching oxide, we turned our attention to details of the more complex reset process, which shows an interesting analogue behaviour.

## V. NATURAL CONDUCTANCE BOUNDARY BETWEEN HRS AND LRS

We have previously reported that bipolar  $\text{SiO}_x$  MOS RRAM devices in the low resistance state can be moved to increasingly higher and higher conductance (set) states by applying progressively higher voltage sweeps.<sup>16</sup> In contrast, we find that such analogue modulation of conductance in MIM structures is seen during the reset process, in which case increasing the voltage sweep reduces the device conductance as the conductive filament is gradually disrupted. Figure 6(a) shows such progressive changes in conductance (expressed as a multiple of the conductance quantum  $G_0$ ) during a gradual reset process. Here, conductance is calculated simply as  $I/V$ , where  $I$  is measured current and  $V$  is the sourced voltage. Starting from the low resistance state, the device is swept to successively higher voltages, from 1.6 V to 2.5 V. A progressive fall in conductance is seen for the first 8 sweeps (1–8). We note that the conduction of these states is nonlinear, which we assign, as in our previous work,<sup>25,26</sup> to the existence of parallel conduction paths (a

linear component coming from the conductive filament, and a non-linear component from surrounding partially formed semiconducting tissue) or a residual potential barrier between the oxide and the contact. Such a gradual reduction in conductance is consistent with a progressive thinning of an initially robust conductive filament by thermally driven re-oxidation of a weak switching point. As this thinning approaches the limit at which there is a single conductive channel, any further re-oxidation of the weak point of the filament will result in an abrupt drop in conductance, as is seen at a bias of  $\sim 2.8$  V (sweep 9). It is significant that at this point the device conductance drops to  $G_0$ . Beyond this point, no further reset transitions were seen in our samples and this may be taken to be the final reset, or high resistance, state of the device. Not that we are not focusing on quantised conduction *per se*, but rather the dynamics of the reset process, more specifically the end of the reset process and the boundary between the final conductance state and conductances of the intermediate states.

The I/V characteristics can be understood as arising from changes in both the conductive filament and the surrounding partially conductive tissue. Each experiences reduction in conductance as it is progressively re-oxidised. However, only the filament shows quantised behaviour, as its dimensions are sufficiently small to allow it to be considered as a quantum point contact. Electron transport at the quantum constriction is ballistic, and conductance is quantised in multiples of  $G_0$  as demonstrated in our previous study.<sup>23</sup> On the other hand, the surrounding tissue is rather poorly spatially defined, and provides background conduction due to processes such as trap assisted tunnelling between defect states. No quantisation is seen in the high resistance state because there is no quantum constriction, and hence no

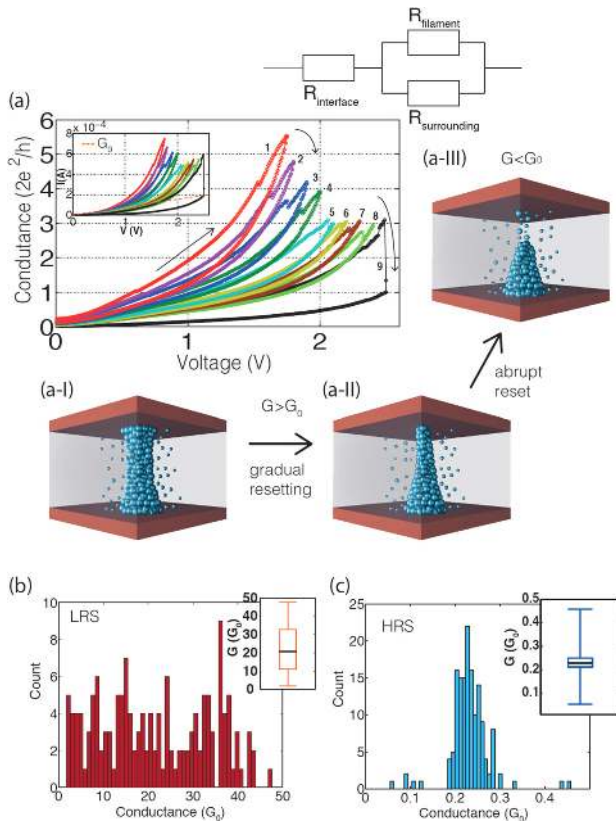


FIG. 6. (a) Gradual modification of device conductance during the reset process. Top right corner: Equivalent circuit model. Abrupt transitions are seen once the conductance goes below  $G_0$ . (a-I) and (a-II) schematically show the filament thinning during the gradual reset, and (a-III) shows the formation of a filament gap once the abrupt current drop is observed. (b) and (c) Distribution of conductance in (b) LRS and (c) HRS over 150 switching events. Insets: the box plots for both LRS and HRS. The band inside the box is the median value. The top and the bottom of the box represent are 25th and 75th percentiles, respectively. The two whiskers are the maximum and the minimum values of the state conductance.

ballistic transport. As the tissue is re-oxidised, we see a monotonic decrease in background (non-linear) conductance.

We may further explain the lower conductance at smaller biases by the presence of a Schottky barrier or tunnelling gap between the switching oxide and contacts. The equivalent circuit model is shown in Figure 6(a) (top right corner).  $R_{\text{interface}}$  represents the resistance due to a Schottky/tunnelling barrier. This resistance acts as a conductance bottleneck at lower voltages but does not significantly affect conductance at higher voltages.  $R_{\text{filament}}$  and  $R_{\text{surrounding}}$  represent two resistances of two parallel paths (filament resistance and resistance coming from leakage from the whole contact area). This model is explained in more detail in our previous study.<sup>24,27</sup> Figures 6(a-I)–6(a-III) summarise our postulated mechanism. Steady re-oxidation of the conductive filament and radial shrinking of the filament at the switching point is shown in Figures 6(a-I)–6(a-II). This process continues until a gap in the filament is produced, accompanied by a sharp current drop in the I-V characteristics (line 9 in Figure 6(a)). The end of the reset process is observed once the overall conductance goes below the level of  $G_0$  and the tip of the filament is disrupted (Figure 6(a-III)). To further

test this hypothesis, we analysed the conductances of the high and low resistance states over 150 switching events. Figures 6(b) and 6(c) show that the conductance of the LRS is distributed between  $1.7 G_0$  and  $47.6 G_0$  (median value  $20.7 G_0$ ); no values below  $G_0$  are seen, while that of the HRS ranges from  $0.05 G_0$  to  $0.45 G_0$  (median value  $0.23 G_0$ ), suggesting  $G_0$  as the natural boundary between the two states. A similar result was reported in the  $\text{TiO}_x$  system.<sup>28</sup> The high resistance state is defined by the presence of a gap within the conductive filament and the low resistance state is defined by fully formed (unbroken) filament, regardless of filament thickness. It is evident that the conductance distribution of the high resistance state is narrower than that of the low resistance state. This is in contrast to conventional metal oxide RRAM devices, in which the distribution of the LRS is typically narrower than that of the HRS. A possible explanation is that, even in the LRS, there is a non-zero potential barrier between the end of the filament and the contact. Any small variation of the barrier height or width affects the resistance of the LRS, and hence we see cycle-to-cycle variation of the resistance due to conformational changes in the filament. This is also consistent with the observation that the LRS shows nonlinear conduction (in contrast to conventional metal oxides, which typically have a linear LRS). In the case of the HRS, it is likely that the device resistance is determined mostly by the bulk conduction rather than the residual filament conduction. Bulk conduction is expected to remain similar from cycle to cycle.

Similar results have been reported for hafnium oxide-based RRAM devices, in which case a clear difference between three conduction states is seen (a first state where  $G \gg G_0$ , corresponding the fully formed filament, a second state where  $G \approx G_0$ , corresponding to filament thinning and a third state where  $G < G_0$ , corresponding to the broken filament).<sup>29</sup> To our knowledge, this is the first report of this effect in  $\text{SiO}_x$  RRAM devices.

## VI. SUMMARY

In summary, we have studied resistive switching in  $\text{SiO}_x$  MIM RRAM devices in which switching is intrinsic to the oxide, due to the formation of conductive filaments generated by the movement of oxygen ions. The switching phenomena hence result from the intrinsic formation of conductive pathways within the  $\text{SiO}_x$ , and not due to extrinsic factors such as metallic filaments as have been reported for metal-diffused  $\text{SiO}_x$  layers. Equally, switching occurs in the bulk of the oxide rather than at the surface due to the formation of silicon filaments. At this time, we do not know the composition of the filaments, only that they are intrinsic to the oxide. We have used AFM, C-AFM, SIMS, and XPS to examine the structural changes occurring during the switching process. We observed bubbles forming at the surface of  $\text{SiO}_x$  during switching, with those resulting from a positive form being significantly more elastic than those from a negative form. We explain this by movement of oxygen ions and the sub-surface accumulation of molecular oxygen, causing distortion of the sample surface. We also highlight the significance of the conductance quantum,  $G_0$ , as the natural



boundary between the high and low resistance states, and hence a quick test for the completion of the reset process. This can have important implications for device endurance and appropriate choice of the switching regime (e.g., current compliance).

- <sup>1</sup>R. Waser and M. Aono, *Nat. Mater.* **6**(11), 833–840 (2007).
- <sup>2</sup>A. Mehonic, S. Cuff, M. Wojdak, S. Hudziak, O. Jambois, C. Labbé, B. Garrido, R. Rizk, and A. J. Kenyon, *J. Appl. Phys.* **111**, 074507 (2012).
- <sup>3</sup>A. C. Torrezan, J. P. Strachan, G. Medeiros-Ribeiro, and R. S. Williams, *Nanotechnology* **22**(48), 485203 (2011).
- <sup>4</sup>H. Y. Chen, S. Yu, B. Gao, P. Huang, J. Kang, and H.-S. P. Wong, in *2012 IEEE International Electron Devices Meeting (IEDM)* (IEEE, 2012), pp. 20.7.1–20.7.7.
- <sup>5</sup>C. Schindler, G. Staikov, and R. Waser, *Appl. Phys. Lett.* **94**(7), 072109 (2009).
- <sup>6</sup>T. M. Tsai, K. C. Chang, T. C. Chang, G. W. Chang, Y. E. Syu, Y. T. Su, G. R. Liu, K. H. Liao, M. C. Chen, H. C. Huang, Y. H. Tai, D. S. Gan, C. Ye, H. Wang, and S. M. Sze, *IEEE Electron Device Lett.* **33**(12), 1693 (2012).
- <sup>7</sup>B. J. Choi, A. C. Torrezan, K. J. Norris, F. Miao, J. P. Strachan, M. X. Zhang, D. A. A. Ohlberg, N. P. Kobayashi, J. J. Yang, and R. S. Williams, *Nano Lett.* **13**(7), 3213 (2013).
- <sup>8</sup>S. Tappertzhofen, H. Mündelein, I. Valov, and R. Waser, *Nanoscale* **4**(10), 3040–3043 (2012).
- <sup>9</sup>K. C. Chang, T. M. Tsai, T. C. Chang, H. H. Wu, J. H. Chen, Y. E. Syu, G. W. Chang, T. J. Chu, G. R. Liu, Y. T. Su, M. C. Chen, J. H. Pan, J. Y. Chen, C. W. Tung, H. C. Huang, Y. H. Tai, D. S. Gan, and S. M. Sze, *IEEE Electron Device Lett.* **34**(3), 399 (2013).
- <sup>10</sup>D. R. Lamb and P. C. Rundle, *Br. J. Appl. Phys.* **18**, 29 (1967).
- <sup>11</sup>C. M. Osburn and D. W. Ormond, *J. Electrochem. Soc.* **119**, 591 (1972).
- <sup>12</sup>A. D. Pearson and C. E. Miller, *Appl. Phys. Lett.* **14**, 280 (1969).
- <sup>13</sup>J. Yao, Z. Sun, L. Zhong, D. Natelson, and J. M. Tour, *Nano Lett.* **10**, 4105 (2010).
- <sup>14</sup>Y. Wang, Y. Chen, F. Xue, F. Zhou, Y. Chang, B. Fowler, and J. Lee, *Appl. Phys. Lett.* **100**, 083502 (2012).
- <sup>15</sup>Y. Chang, P. Chen, Y. Chen, F. Xue, Y. Wang, F. Zhou, B. Fowler, and J. Lee, *Appl. Phys. Lett.* **101**, 052111 (2012).
- <sup>16</sup>A. Mehonic, S. Cuff, M. Wojdak, S. Hudziak, O. Jambois, C. Labbé, B. Garrido, R. Rizk, and A. J. Kenyon, *Nanotechnology* **23**(45), 455201 (2012).
- <sup>17</sup>Y. Wang, X. Qian, K. Chen, Z. Fang, W. Li, and J. Xu, *Appl. Phys. Lett.* **102**, 042103 (2013).
- <sup>18</sup>Y.-F. Chang, B. Fowler, Y.-C. Chen, Y.-T. Chen, Y. Wang, F. Xue, F. Zhou, and J. C. Lee, *J. Appl. Phys.* **116**, 043708 (2014).
- <sup>19</sup>Y.-F. Chang, B. Fowler, Y.-C. Chen, Y.-T. Chen, Y. Wang, F. Xue, F. Zhou, and J. C. Lee, *J. Appl. Phys.* **116**, 043709 (2014).
- <sup>20</sup>G. Wang, A. R. O. Raji, J. H. Lee, and J. M. Tour, *ACS Nano* **8**(2), 1410 (2014).
- <sup>21</sup>D. H. Kwon, K. M. Kim, J. H. Jang, J. M. Jeon, M. H. Lee, G. H. Kim, X. S. Li, G. S. Park, B. Lee, S. Han, M. Kim, and C. S. Hwang, *Nat. Nanotechnol.* **5**, 148 (2010).
- <sup>22</sup>J. J. Huang, C. W. Kuo, W. C. Chang, and T. H. Hou, *Appl. Phys. Lett.* **96**, 262901 (2010).
- <sup>23</sup>J. J. Yang, F. Miao, M. D. Pickett, D. A. A. Ohlberg, D. R. Stewart, C. N. Lau, and R. S. Williams, *Nanotechnology* **20**, 215201 (2009).
- <sup>24</sup>*Nanoelectronics and Information Technology*, edited by R. Waser (John Wiley and Sons, 2012), p. 700.
- <sup>25</sup>A. Mehonic, A. Vrajitoarea, S. Cuff, S. Hudziak, H. Howe, C. Labbé, R. Rizk, M. Pepper, and A. J. Kenyon, *Sci. Rep.* **3**, 2708 (2013).
- <sup>26</sup>E. Miranda, A. Mehonic, J. Suñé, and A. J. Kenyon, *Appl. Phys. Lett.* **103**, 222904 (2013).
- <sup>27</sup>E. Miranda, A. Mehonic, J. Blasco, J. Suñé, and A. J. Kenyon, *IEEE Trans. Nanotechnol.* **14**, 15 (2015).
- <sup>28</sup>C. Hu, M. D. McDaniel, A. Posadas, A. A. Demkov, J. G. Ekerdt, and E. T. Yu, *Nano Lett.* **14**(8), 4360–4367 (2014).
- <sup>29</sup>S. Long, L. Perniola, C. Cagli, J. Buckley, X. Lian, E. Miranda, F. Pan, M. Liu, and J. Suñé, *Sci. Rep.* **3**, 2929 (2013).